# A Superflare on YZ Canis Minoris Observed by the Seimei Telescope and TESS: Red Asymmetry of Hα Emission Associated with White-light Emission



Namizaki, Keiichi; Namekata, Kosuke; Maehara, Hiroyuki; Notsu, Yuta; Honda, Satoshi; Nogami, Daisaku; Shibata, Kazunari



2023-03-01

The Astrophysical Journal, 945:61 (9pp), 2023 March 1 https://doi.org/10.3847/1538-4357/acb928


# A Superflare on YZ Canis Minoris Observed by the Seimei Telescope and TESS: Red Asymmetry of Hα Emission Associated with White-light Emission

Keiichi Namizaki[1], Kosuke Namekata[2], Hiroyuki Maehara[3], Yuta Notsu[4,5,6], Satoshi Honda[7], Daisaku Nogami[1,8], and Kazunari Shibata[9,10]

[1] Department of Astronomy, Kyoto University, Kitashirakawa-Oiwake-cho, Sakyo-ku, Kyoto 606-8502, Japan; namizaki@kusastro.kyoto-u.ac.jp
[2] ALMA Project, NAOJ, NINS, Osawa, Mitaka, Tokyo 181-8588, Japan
[3] Okayama Branch Office, Subaru Telescope, NAOJ, NINS, Kamogata, Asakuchi, Okayama 719-0232, Japan
[4] Laboratory for Atmospheric and Space Physics, University of Colorado Boulder, 3665 Discovery Drive, Boulder, CO 80303, USA
[5] National Solar Observatory, 3665 Discovery Drive, Boulder, CO 80303, USA
[6] Department of Earth and Planetary Sciences, Tokyo Institute of Technology, 2-12-1 Ookayama, Meguro-ku, Tokyo 152-8551, Japan
[7] Nishi-Harima Astronomical Observatory, Center for Astronomy, University of Hyogo, Sayo, Hyogo 679-5313, Japan
[8] Astronomical Observatory, Kyoto University, Sakyo, Kyoto 606-8502, Japan
[9] Kwasan Observatory, Kyoto University, Yamashina, Kyoto 607-8471, Japan
[10] School of Science and Engineering, Doshisha University, Kyotanabe, Kyoto 610-0321, Japan
*Received 2022 May 24; revised 2023 February 3; accepted 2023 February 3; published 2023 March 7*

## Abstract

Active M-type stars are known to often produce superflares on the surface. Radiation from stellar (super)flares is important for exoplanet habitability, but the mechanisms are not well understood. In this paper, we report simultaneous optical spectroscopic and photometric observations of a stellar superflare on an active M dwarf, YZ Canis Minoris, with the 3.8 m Seimei telescope and the Transiting Exoplanet Survey Satellite. The flare bolometric energy is $1.3^{+1.6}_{-0.6} \times 10^{34}$ erg and the Hα energy is $3.0^{+0.1}_{-0.1} \times 10^{32}$ erg. The Hα emission line profile shows red asymmetry throughout the flare, with a duration of 4.6–5.1 hr. The velocity of the red asymmetry is ∼200–500 km s$^{-1}$ and the line width of Hα broadens up to 34 ± 14 Å. The redshifted velocity and line width of Hα line decay more rapidly than the equivalent width, and their time evolutions are correlated with that of the white-light emission. This indicates the possibility of the white light, the Hα red asymmetry, and the Hα line broadening originating from nearly the same site, i.e., the dense chromospheric condensation region, heated by nonthermal electrons. On the other hand, the flux ratio of the redshifted excess components to the central components is enhanced one hr after the flare's onset. This may be due to the main source of the red asymmetry changing to post-flare loops in the later phase of the flare.

*Unified Astronomy Thesaurus concepts:* Stellar flares (1603); Stellar phenomena (1619); Optical flares (1166); Solar flares (1496); Magnetic variable stars (996); M dwarf stars (982); Solar magnetic reconnection (1504); Solar magnetic fields (1503); Magnetic fields (994)

## 1. Introduction

Solar and stellar flares are known to be explosive phenomena that occur on the solar and stellar surface. Flares are observed as rapid increases in a wide range of electromagnetic radiation, from gamma rays to radio waves. The mechanism for producing solar and stellar flares is thought to be related to magnetic reconnection in the coronal region (e.g., Shibata & Yokoyama 2002; Shibata & Magara 2011; Namekata et al. 2017). The magnetic energy that is stored around spots is converted into thermal, nonthermal, and kinetic energy via magnetic reconnection (e.g., Notsu et al. 2013; Shibata et al. 2013). In the case of solar flares, the released energy is typically $10^{29}$–$10^{32}$ erg (e.g., Shibata & Magara 2011; Emslie et al. 2012). On the other hand, some of the stellar flares release more than 10 times the energy of the largest solar flares, which are called superflares (e.g., Maehara et al. 2012; Shibayama et al. 2013; Candelaresi et al. 2014; Hawley et al. 2014; Davenport 2016; Notsu et al. 2019; Okamoto et al. 2021). Recently, there has been increasing interest in how these stellar superflares affect the habitability of exoplanets, and how and whether the superflares on the Sun can affect the Earth (Shibata et al. 2013; Airapetian et al. 2016; Yamashiki et al. 2019).

In the standard model of solar flares, the released energy is transported to the chromosphere and photosphere through thermal conduction and accelerated nonthermal energetic particles. The transported energy increases the temperature and gas pressure in the upper chromosphere and ionizes the atoms, resulting in chromospheric emission, such as Hα line (Priest & Forbes 2002). The heated hot plasma, with a temperature of $10^7$ K, flows upward into the coronal magnetic loop, which is called chromospheric evaporation (Fisher et al. 1985). On the other hand, as a backreaction from the upward chromospheric evaporation, downward flows of chromospheric plasmas ($10^4$ K) also occur, and this is called chromospheric condensation. Some aspects of this standard theory can be seen in the following solar Hα observations. At the footpoints of the flaring magnetic loops, the Hα line is often symmetrically broadened, in association with flares (e.g., Svestka 1962, 1963; Johns-Krull et al. 1997). This broadening is thought to be mainly caused by electric microfield pressure broadening (the Stark effect), indicating an enhanced electron density in the chromosphere, or perhaps by magnetic turbulent broadening (e.g., Kowalski et al. 2017b; Fuhrmeister et al. 2018). In addition, the redshifted components in the Hα line are often observed at the footpoints, in a process called red asymmetry (e.g., Švestka et al. 1962; Janssens & White 1970;

Hanaoka 2003; Asai et al. 2012). The generation mechanism of the red asymmetry is thought to be downward chromospheric condensation (e.g., Ichimoto & Kurokawa 1984; Canfield et al. 1990). This is usually observed in the impulsive phases of solar flares. Post-flare loops are another cause of the redshifted components in H$\alpha$, as the evaporated plasmas that become cool and dense in the coronal magnetic loops fall into the chromosphere along magnetic field lines (e.g., Bruzek 1964). The red asymmetry of H$\alpha$ due to post-flare loops generally occurs in the decay phases of flares, since it requires a cooling time due to the thermal radiation and conduction (e.g., Claes & Keppens 2019; Claes et al. 2020).

Unlike solar observations, stellar flares have mainly been investigated through photometric observations (e.g., Kowalski et al. 2009; Hawley et al. 2014; Chang et al. 2015; Davenport 2016), so there are not many spectroscopic observations, especially for superflares. For example, there is a difference of more than two orders of magnitude between the number of flares observed by photometry in one paper (e.g., >100,000, in Davenport 2016) and spectroscopy in another (e.g., ∼10–100, in Kowalski et al. 2013; Namekata et al. 2020). The red asymmetry of chromospheric lines is sometimes observed in stellar flares. For example, Houdebine et al. (1993) reported red asymmetries of the Balmer lines during the flare of an M dwarf, AD Leo, while Fuhrmeister et al. (2018) found red asymmetries in 32 snapshot frames of the flare or quiescent states of 28 M dwarfs. Furthermore, Wu et al. (2022) have investigated the time evolution of the red asymmetry and line width of the H$\alpha$ line during a flare on an M4-type star, reporting that both decay more rapidly than the H$\alpha$ equivalent width (EW). They interpret these features as evidence of flare-driven coronal rain, chromospheric condensation, or a filament or prominence eruption, either with a nonradial backward propagation or with strong magnetic suppression. However, it is not yet known whether the origins of red asymmetry can be explained by the same model as for solar flares, since stellar flares cannot be spatially resolved and the observed red asymmetry could result from a superposition of various phenomena.

Another large challenge for solar and stellar flares involves the origin of the visible continuum emission in the flares that are called white-light flares. The mechanism has been controversial, although the white-light emission is important in solar- and stellar-flare physics, since the released flare energy is largely distributed as white-light flare energy (Kretzschmar 2011). Based on solar observations, the following possible emission mechanisms have been proposed: (1) radiation from the chromosphere is heated and condensed by nonthermal electrons (e.g., Ichimoto & Kurokawa 1984); (2) radiation from the photosphere heated by high-energy protons (e.g., Najita & Orrall 1970); or (3) re-radiation occurs through radiative backwarming (e.g., Machado et al. 1989). According to solar observations, the similarities between the light curves and spatial locations of hard X-rays and white-light flares suggest that the white-light emission is related to nonthermal electrons (e.g., Hudson et al. 2006; Krucker et al. 2011). However, possibilities (1) and (3) have not been constrained, since observations of the heights and spectra of solar white-light flares are not so easy. In the case of stellar white-light flares, broadband spectra are often reported for M dwarfs, since the stars themselves are darker than the Sun and the energy scale of flare is very large. For example, Hawley & Fisher (1992) reported a continuum spectrum during a superflare on a mid-M dwarf, AD Leo, with a blackbody spectrum of the temperature of 8500–9500 Kowalski et al. (2010, 2013, 2016) have reported a variety of broadband white-light spectra on active M dwarfs, suggesting that the variety can be explained by the radiation from the chromosphere being heated and condensed by nonthermal electrons. Namekata et al. (2020) found a correlation between the white-light emission and H$\alpha$ line broadening during a superflare on AD Leo, indicating a possible connection between the white-light emission and chromospheric condensation. Simultaneous spectroscopic observations of the H$\alpha$ line can be an important tool for unveiling the radiation mechanism of the white-light emissions of flares.

In this paper, we report spectroscopic and photometric observations of a superflare on an active M dwarf, YZ Canis Minoris (YZ CMi), with high precision and high temporal resolution, using the Seimei telescope (Kurita et al. 2020) and the Transiting Exoplanet Survey Satellite (TESS; Ricker et al. 2015). As a result, we find a possible connection between the H$\alpha$ red asymmetry and the white-light emission for this superflare, which could provide an opportunity for unveiling the mechanism of the red asymmetry and the white-light emission at the same time. The data, observations, and analysis methods are described in Section 2. The results are described in Section 3.1, and we also discuss the time variation of the line broadening (Section 3.2) and the red asymmetry in the H$\alpha$ line with that of the white light (Section 3.3). A summary and future works are described in Section 4.

## 2. Observations and Analyses

### 2.1. Target Star: YZ CMi

The active M4.5 dwarf YZ CMi has a thick convection zone and a rapid rotation, with a period of 2.8 days, which results in a high flare frequency (e.g., Morin et al. 2008). Numerous flares on YZ CMi have been observed over a wide range of wavelengths, from radio to X-ray, since the first flare in this object was observed by van Maanen (1945). In particular, a superflare with a $U$-band energy of $\sim 10^{34}$ erg was reported in Kowalski et al. (2010). Lacy et al. (1976) and Maehara et al. (2021) have measured the flare frequency distribution for YZ CMi and found that its power-law index is comparable to those of other M-type stars as well as the Sun.

### 2.2. TESS

TESS performed optical photometric observations of YZ CMi in the wavelength range 6000–10,000 Å, which were simultaneous with our ground-based spectroscopic observations. TESS was launched in 2018 April and it has four cameras covering $24° \times 96°$ degree strips of the sky, called "Sectors." Each Sector observes an area for about 27 days, on average, and the data that are obtained by TESS are of very high precision. The TESS observation for Sector 34 was performed from 2021 January 14 to 2021 February 8 (Barycentric Julian Date, or BJD: 2459229.09–2459254.07). In Sector 34, TESS observed YZ CMi with a 20 s cadence. We analyzed the TESS Pre-search Data Conditioned Simple Aperture Photometry light curves, which were retrieved from the MAST Portal website.[11] The normalized TESS light curve shown in Figure 1(a) displays rotational brightness variations

[11] https://mast.stsci.edu/portal/Mashup/Clients/Mast/Portal.html

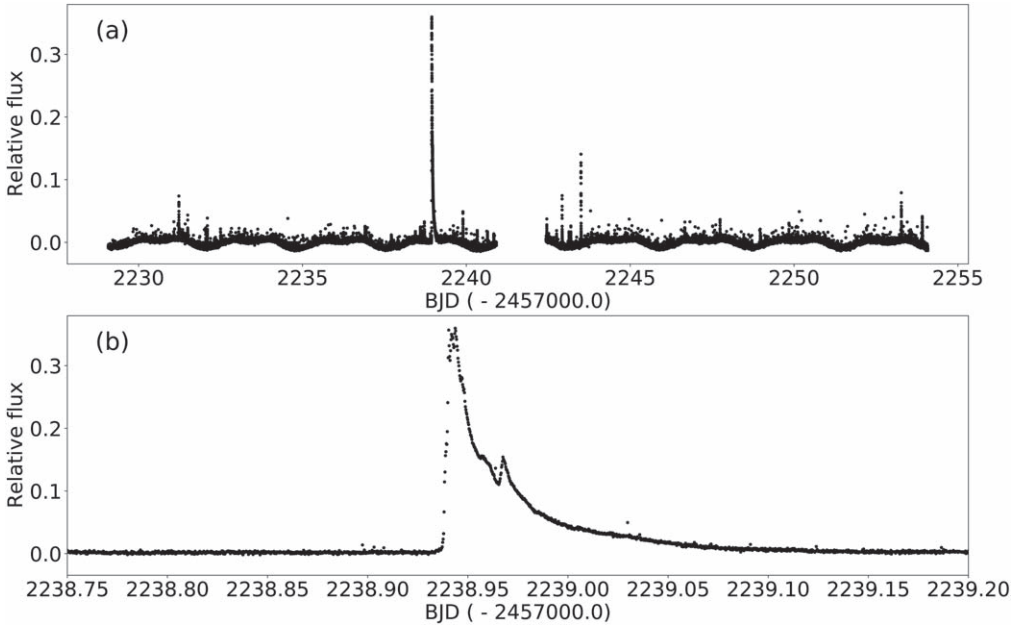


**Figure 1.** Light curve of YZ CMi observed with the TESS 20 s cadence mode. (a) The full light curve during Sector 34. The horizontal and vertical axes represent the observation time in BJD and the relative flux normalized by the average flux ($\delta F/F_{\rm av}$), respectively. (b) Enlarged light curve around the superflare analyzed in this paper.

and rapid flares, while Figure 1(b) presents an expanded panel showing a superflare of interest to this paper.

From the TESS light curve, we estimate the energy of the white-light flare by assuming 10,000 K blackbody radiation (Shibayama et al. 2013). First of all, the flare flux ($\delta F$) normalized by the averaged stellar flux ($F_{\rm av}$) can be expressed as the ratio of the flare luminosity to the stellar luminosity, as follows:

$$\frac{\delta F}{F_{\rm av}} = \frac{A_{\rm flare}}{\pi R_{\rm star}^2} \frac{\int R_\lambda B_\lambda(T_{\rm flare})d\lambda}{\int R_\lambda B_\lambda(T_{\rm eff})d\lambda}, \quad (1)$$

where $\delta F/F_{\rm av}$ is the relative flux, $R_\lambda$ is the response function of the TESS detector, $R_{\rm star}$ is the radius of YZ CMi ($\sim 0.3\,R_{\rm solar}$), $A_{\rm flare}$ is the flaring area, $T_{\rm eff}$ is the stellar effective temperature of $\sim$3300 K (Gaidos & Mann 2014; Newton et al. 2015; Houdebine et al. 2016), $T_{\rm flare}$ is the flare temperature of 10,000 $\pm$ 5000 K (e.g., Hawley & Fisher 1992; Howard et al. 2020), and $B_\lambda$ is the Planck function. After deriving the flaring area based on Equation (1), we calculate the flare luminosity, using the following equation:

$$L_{\rm flare} = \sigma T_{\rm flare}^4 A_{\rm flare}, \quad (2)$$

where $\sigma$ is the Stefan–Boltzmann constant. By integrating the flare luminosity along time, the bolometric energy of the superflare ($E_{\rm bol}$) is obtained. Since $E_{\rm bol}$ is mainly dependent on $T_{\rm flare}$, the uncertainty of $E_{\rm bol}$ is estimated mainly by considering the error of $\pm$ 5000 K (Howard et al. 2020). In addition, the duration of the white-light flare is calculated as the decay time, which is one-tenth of the peak in the light curve.

### 2.3. 3.8 m Seimei Telescope

We performed spectroscopic observations of YZ CMi with the 3.8 m Seimei telescope, which is located at Okayama Observatory, Japan. The Seimei telescope is equipped with a low-dispersion spectrograph, KOOLS-IFU (the Kyoto Okayama Optical Low-dispersion Spectrograph, with an optical fiber Integral Field Unit; Matsubayashi et al. 2019). We used the VPH683 grism, covering the wavelength range of 5800–8000Å, with a spectral resolution of $\lambda/\Delta\lambda \sim 2000$. This wavelength coverage includes the H$\alpha$ line (6562.8 Å), which is a chromospheric line that is often used as a tracer of flaring activity. The exposure time was 60 s and the CCD readout time was about 17 s. These spectroscopic observations with such a high temporal resolution allow us to investigate the temporal variation of the H$\alpha$ spectrum during stellar flares in detail.

With the aim of investigating the correspondence between the white light and H$\alpha$ in stellar flares, we performed simultaneous observations of YZ CMi in accordance with TESS Sector 34. The data reduction follows the prescription in Namekata et al. (2020, 2022b, 2021), with the IRAF and PyRAF packages, and each spectrum is calibrated by considering the radial velocity of YZ CMi (26.495 km s$^{-1}$; Soubiran et al. 2018). From the H$\alpha$ line profile, we measure the H$\alpha$ EW, which is the H$\alpha$ emission integrated for 6562.8 $\pm$ 15 Å, after being normalized by the nearby continuum level, and then we plot the light curve in Figure 2. In addition, the H$\alpha$ flux at each time is calculated simply by multiplying the EW by the continuum flux near the H$\alpha$. The continuum flux is obtained by using a flux-calibrated quiescent spectrum (Kowalski et al. 2013), and the same parameters are used when deriving the bolometric energy. The H$\alpha$ energy of the flare ($E_{\rm H\alpha}$) and its uncertainty are then derived by integrating it along the time, considering the error of $T_{\rm flare}$. Furthermore, the duration of the H$\alpha$ flare is calculated as the decay time for the H$\alpha$ EW to decay to the quiescent level with $1\sigma$ or $5\sigma$, which is the standard deviation of the residuals.

### 2.4. Analysis of Red Asymmetry and Line Broadening of H$\alpha$ Line Profile

We here introduce the analysis of the fitting of the flare spectrum, in order to characterize the line broadening and asymmetry of the H$\alpha$ line in stellar flares. The example flare

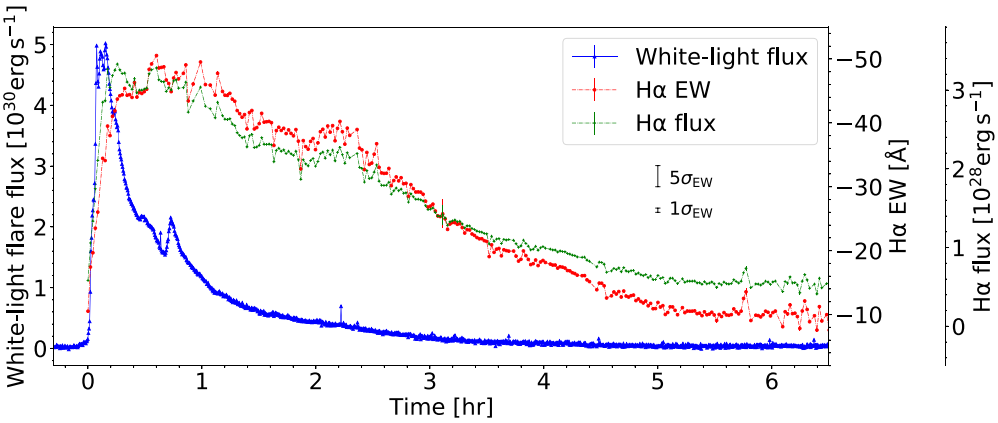


**Figure 2.** Light curves of the H$\alpha$ and white-light emission of the superflare on YZ CMi. The solid blue line scaled on the left vertical axis represents the TESS white-light flare flux in units of erg s$^{-1}$. The red and green dashed–dotted lines represent the H$\alpha$ EW and the H$\alpha$ flux, respectively. The horizontal axis indicates the time since the flare's onset (BJD −2459238.937) in units of hr. The middle and rightmost vertical axes indicate the EW of H$\alpha$ in units of Å and the H$\alpha$ flux in units of erg s$^{-1}$. The error bars of the H$\alpha$ EW and the H$\alpha$ flux are derived from the residual scattering in the line wing. The 1$\sigma_{EW}$ and 5$\sigma_{EW}$ error bars, where $\sigma_{EW}$ of 0.7 Å is the standard deviation of the light curve of H$\alpha$ in the quiescent phase (around 6 hr after the flare's onset), are also shown.

spectra are shown in Figure 3. We normalize the H$\alpha$ line profile by the continuum level and subtract the quiescence spectrum (the dotted gray line in Figure 3(b)) from the flare spectra (e.g., the solid green and dashed blue lines in Figure 3(b)). Here, we take for the quiescence spectrum the spectrum at around 6 hr in Figure 2, since the EW at this time and those on other days, when flares did not occur, are at nearly the same level. We then obtain the time variation of the quiescence level–subtracted H$\alpha$ line profile as in Figures 3(c) and (d).

We derive the line width and the velocity of the asymmetric components. In the following, we introduce the fitting method when the flare spectrum shows a redshifted component in the H$\alpha$ wing. First, we fit only the blueward line profile from the H$\alpha$ line center with a Voigt function (see the solid red line in Figure 4), with the aim of simply estimating the line profile without a redshift component. The function obtained by fitting the blueward line profile is folded back to the red side at the H$\alpha$ line center (see the solid red line in Figure 4). We then subtract the obtained symmetrically broadened line (i.e., the model of a nonmoving spectrum with a velocity of 0) from the observed line profile (the blue points in Figure 4). The resulting residuals (the green crosses in Figure 4) in the redward asymmetry are regarded as the "redshifted components" in this study. We again fit a Voigt function to the residuals and estimate the redshifted components (the dashed black lines in Figure 4) with a free parameter of the central velocity. Here, if the central components are fitted simultaneously with redshifted components, the fitting does not work well and the redshifted components are not extracted properly. Thus, we decided to fix the central component before fitting the redshifted components. As a result of this fitting, the line-of-sight redshifted velocity is estimated from the Doppler shift of the redward residual components (the dashed black lines in Figure 4). The EW is also calculated for the central components and the redshifted components by simply integrating along the wavelengths, and their ratio is also obtained. This method is applied to each spectrum that was observed with a time interval of ∼77 s. Spectra showing "blue asymmetry" can be fitted in the same way, but we could not see the "blue asymmetry" in this flare, as will be discussed in Section 3.1. Only the redward excess was evaluated in this study, then.

In addition, with the aim of estimating the blueward and redward line broadening, we perform Voigt function fittings for the blueward and redward line profiles separately. The blueward and redward line widths are calculated by obtaining the wavelengths at one-eighth of the peak intensity for the blue and red sides, respectively. In this paper, we define the central line width (the dotted green line with the cross symbols in Figure 5(a)) as twice the blueward line width (the dotted cyan lines with star symbols in Figure 5(a)).

Futhermore, the decay times of the central line width and redshift velocity are calculated at the times when they decay to one-tenth of the peak. Here, both standard deviations of the residuals ($\sigma_{width}$, $\sigma_{velocity}$) are added to the values of one-tenth of the peak as errors, to estimate the uncertainties of the decay times.

Note that the line width and redshift velocity near the spectral resolution limit of KOOLS-IFU (∼150 km s$^{-1}$) could be overestimated, although the qualitative trend would be real. For this reason, we do not quantitatively discuss the data after 3 hr in Figure 5(c) in this paper.

## 3. Results and Discussion

### 3.1. Summary

Figure 1 shows the TESS light curve of YZ CMi in Sector 34. The flare of interest in this paper is the largest event among those detected by the TESS Sector 34 observations. As shown in Figure 1(b), the white light increases by ∼35% relative to the averaged flux of the quiescence phase. We successfully observed this largest event in TESS Sector 34 with ground-based optical spectroscopic observations. The bolometric energy of the flare ($E_{bol}$) is calculated as $1.3^{+1.6}_{-0.6} \times 10^{34}$ erg, using the method described in Section 2.2; this can be classified as a superflare. Here, it is difficult to constrain $T_{flare}$ by fitting to the spectrum, because of the narrow wavelength range and lack of a near-UV spectrum covered by the VPH683 grism. However, even assuming a 20,000 K blackbody, $E_{bol}$ is $5.5 \times 10^{34}$ erg, and thus it is not significantly dependent on $T_{flare}$. Figure 2 shows the light curves of the superflare in TESS white light and H$\alpha$. It is found that the white-light flare is dominant in the rising phase of the H$\alpha$ EW, and that it decays more rapidly (in 1.6 hr) than the H$\alpha$ flare (in 4.0–4.5 hr). It is

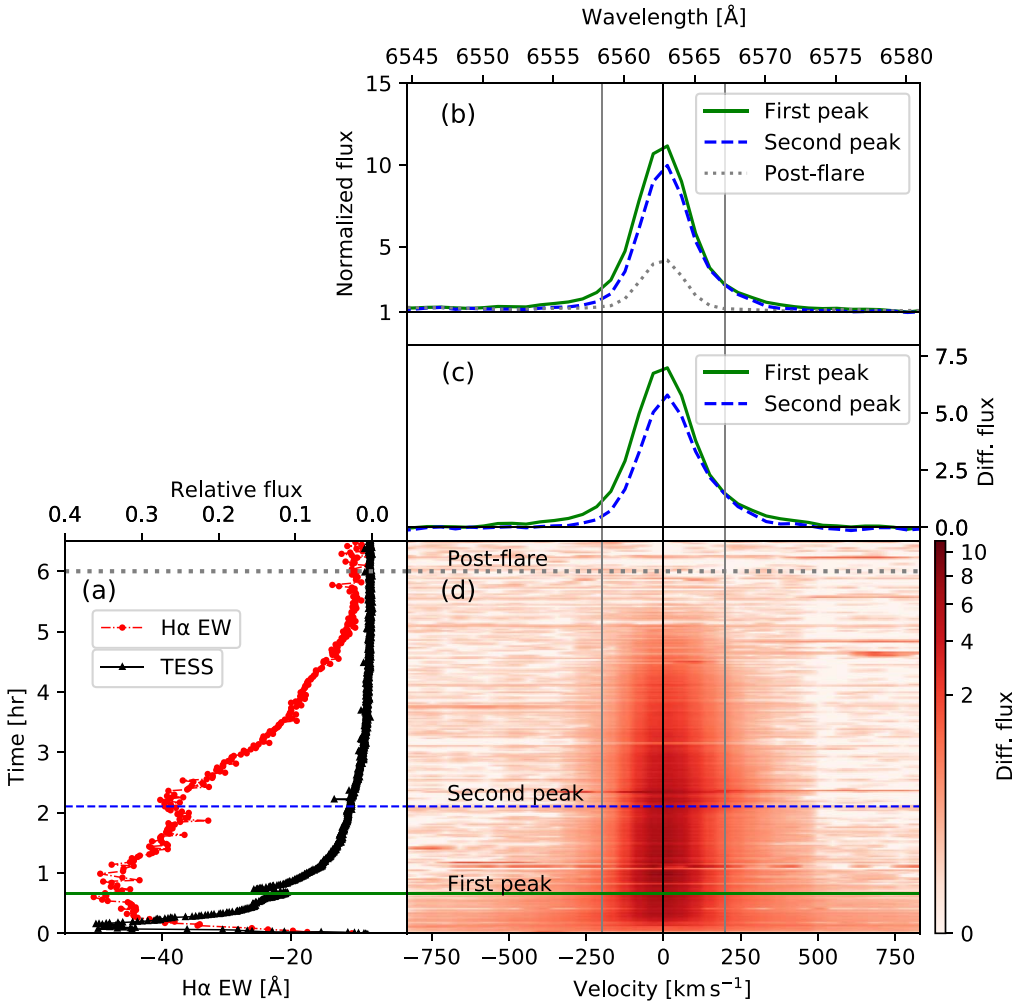


**Figure 3.** Time evolution of the H$\alpha$ spectrum during the superflare on YZ CMi. (a) The filled red circles and black triangles represent the H$\alpha$ EW and the white-light emission, respectively. This is basically the same as Figure 2. (b) H$\alpha$ line profile. The upper horizontal axis is the wavelength and the vertical axis is the flux normalized by the continuum. The quiescent spectrum of YZ CMi is indicated by the dotted gray line (the average of 10 spectra around 6 hr after the flare's onset, which correspond to the horizontal dotted gray lines in panels (a) and (d)). The solid green and dashed blue lines are the H$\alpha$ line profiles 0.67 hr and 2.10 hr after the flare's onset, respectively, which correspond to the horizontal solid green and dashed blue lines in panels (a) and (d). (c) The flare spectra subtracted from the quiescent spectra (in this paper, we simply call these the flare spectra). (d) Time variation of the (quiescent level–subtracted) H$\alpha$ line profile during the flare. The bottom horizontal axis is the Doppler velocity from the H$\alpha$ line center and the vertical axis is the time from the flare's onset, which shares the left vertical axis of (a). The color map represents the differential flux normalized by the continuum level, as in the color bar.

known that white light is sensitive to nonthermal heating and that H$\alpha$ radiation is related to both nonthermal and thermal heating (e.g., Namekata et al. 2020). Therefore, there is a possibility that the observed time decay between the H$\alpha$ and the white light could be an indication of the Neupert effect in solar flares, which is often seen in soft and hard X-ray radiation (Neupert 1968; Dennis & Zarro 1993). The H$\alpha$ energy of the flare ($E_{\mathrm{H}_\alpha}$) is derived as $3.0^{+0.1}_{-0.1} \times 10^{32}$ erg, which is$\sim$2.3% of the bolometric energy of this superflare.

Figure 3 shows the temporal evolution of the H$\alpha$ spectrum. The H$\alpha$ line profile broadens widely in the impulsive phase (hereafter, the "impulsive phase" means the time between 0 hr and $\sim$1 hr from the flare's onset), while it narrows in the decay phase. In addition, red asymmetries can be seen throughout the flare (e.g., Figures 3(c) and (d)). The results of the spectral fitting for the solid blue and dashed green lines in Figure 3 are shown in Figures 4(a) and (b), respectively. For example, the central line width and redshift velocity of Figure 4(a) are estimated as $9.7 \pm 0.5$ Å and $280 \pm 12$ km s$^{-1}$, respectively, and those of Figure 4(b) are estimated as $8.3 \pm 0.4$ Å and $181 \pm 5$ km s$^{-1}$, respectively.

Figure 5 shows the temporal evolution of the fitting parameters of (a) the line width, (b) the redshift velocity, and (c) the EW ratio of the red asymmetry to the central component, in comparison with the white-light flare and H$\alpha$ light curves (the solid blue and red lines). The features are summarized as follows.

(a) The central line width of the H$\alpha$ line peaks at $34 \pm 14$ Å (0.04–0.12 hr after the flare's onset) and decays rapidly to $10.6 \pm 0.4$ Å (one-tenth of the peak value) over 0.6–0.7 hr. We find that the temporal evolution of the central line width is similar to that of the white-light flare, including the small brightness variation, and that it decays more rapidly than the H$\alpha$ EW. Both the blueward and redward wings show the same trend.

(b) The redshift velocity peaks at $482 \pm 40$ km s$^{-1}$ (0.39–0.45 hr after the flare's onset) and decays rapidly to $183 \pm 9$ km s$^{-1}$ (one-tenth of the peak value) over

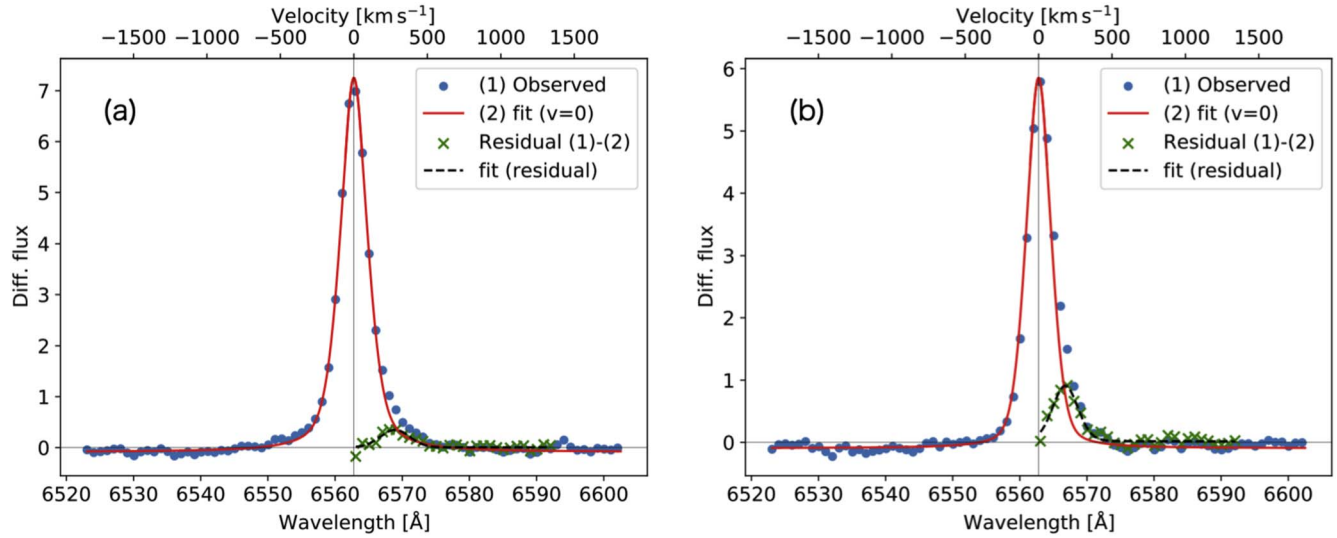


**Figure 4.** Observed H$\alpha$ spectra during the superflare and the fitting results. Panels (a) and (b) represent the spectra indicated by the solid green lines (0.67 hr after the flare's onset) and the dashed blue lines (2.10 hr after the flare's onset) in Figure 3(c). The vertical axis represents the differential flux from the quiescent spectrum. The filled circles represent the observed H$\alpha$ line profiles. The solid red lines are symmetric Voigt functions fitted to the components at shorter wavelengths than the H$\alpha$ line center. The green crosses indicate the residuals of the central Voigt function from the observed lines. The dashed black lines represent the Voigt functions fitted to the residuals (green crosses).

1.6–2.3 hr. The temporal evolution of the redshift velocity is also similar to that of the white-light flare, and it decays more rapidly than the H$\alpha$ EW. This is very similar to the feature of the central line width (a).

(c) The EW ratio of the red asymmetry to the central component is small in the impulsive phase (a few percent) and increases up to ∼20% in the decay phase.

### 3.2. Relation between Line Broadening and White-light Emission

During the impulsive phase (0–1 hr in Figure 5(a)), the H$\alpha$ line is almost symmetrically broadened, in association with the white-light emission. There could be a possible redshifted excess in this impulsive phase, but in the first 20 minutes, the redshifted excess is too weak to be fitted, and therefore we call the profiles in this phase almost symmetric. This means that the line broadening of H$\alpha$ and the white-light emission are related to the same region. The line broadening of H$\alpha$ is often thought to be caused by Stark effect, indicating that the electron density of the chromosphere becomes very high. Namekata et al. (2020) have suggested that line broadening of the H$\alpha$ flare with a width of more than 10 Å cannot be explained by thermal conduction heating alone, but also by nonthermal electron heating of the deep chromosphere. Thus, the line broadening observed in our paper would indicate that the deep chromosphere is heated by nonthermal electrons during this superflare. Furthermore, the time evolution of the central line width of H$\alpha$ and that of the white light show a very good correlation, which suggests that the white-light emission is also radiated from the nonthermally heated chromosphere in this superflare. Kowalski et al. (2015) have simulated and discussed the feasibility of white-light flares being radiated from the chromospheric condensation region in the case of an M-dwarf atmosphere. They found that a photosphere-like dense region was generated in the chromosphere, heated by nonthermal electrons and producing significant white-light emission. As described in the above scenario, our observations suggest the possibility that the white-light emission and the line broadening are produced in the chromosphere, heated by nonthermal electrons during the impulsive phase. Alternatively, it is possible that not only nonthermal electrons, but also nonthermal protons accelerated by flares, may produce a similar behavior, although their properties have not been well studied, either observationally or theoretically. On the other hand, the radiative backwarming scenario (proposed by Machado et al. 1989) would be less likely in this case, because if the backwarming is dominant (and nonthermal heating is less dominant), the time evolution of the white-light flare would be similar to that of the H$\alpha$ flare, because both are heated by the same thermal source in the coronae, i.e., the soft X-ray loops (as proposed by Namekata et al. 2022b), which is different from our observations. The possibility of the radiative backwarming can be further constrained with future simultaneous observations with soft X-rays—the main source of irradiation from the coronae (Nizamov 2019).

Let us discuss the quantitative parameters of this superflare. Namekata et al. (2020) reported a $2 \times 10^{33}$ erg class superflare with strong H$\alpha$ line broadening on an M-type flare star, AD Leo. In the event, the H$\alpha$ emission line's full width at one-eighth of the maximum increased up to 14 Å in the initial phase, showing a slow decay compared to the spiky increase. This feature is similar to our superflare, although the energy scale is a bit different ($1 \times 10^{34}$ erg in our case). Namekata et al. (2020) suggested that the line width could be explained by a nonthermal electron beam of $\sim 10^{12}$ erg cm$^{-2}$ s$^{-1}$ being injected into the chromosphere. On the other hand, our superflare temporarily shows the full width at one-eighth of the maximum of $34 \pm 14$ Å, suggesting an injection of a much higher flux from a nonthermal electron beam. In addition, the central line width dramatically decreases, from $34 \pm 14$ Å in the initial phase to one-tenth of its peak value in the decay phase, within 1 hr. This means that the nonthermal heating also dramatically decreases as the flare decays. Considering that the variation timescale is very long (0.6–0.7 hr) compared to the flare heating timescale at a given flare ribbon as seen in solar

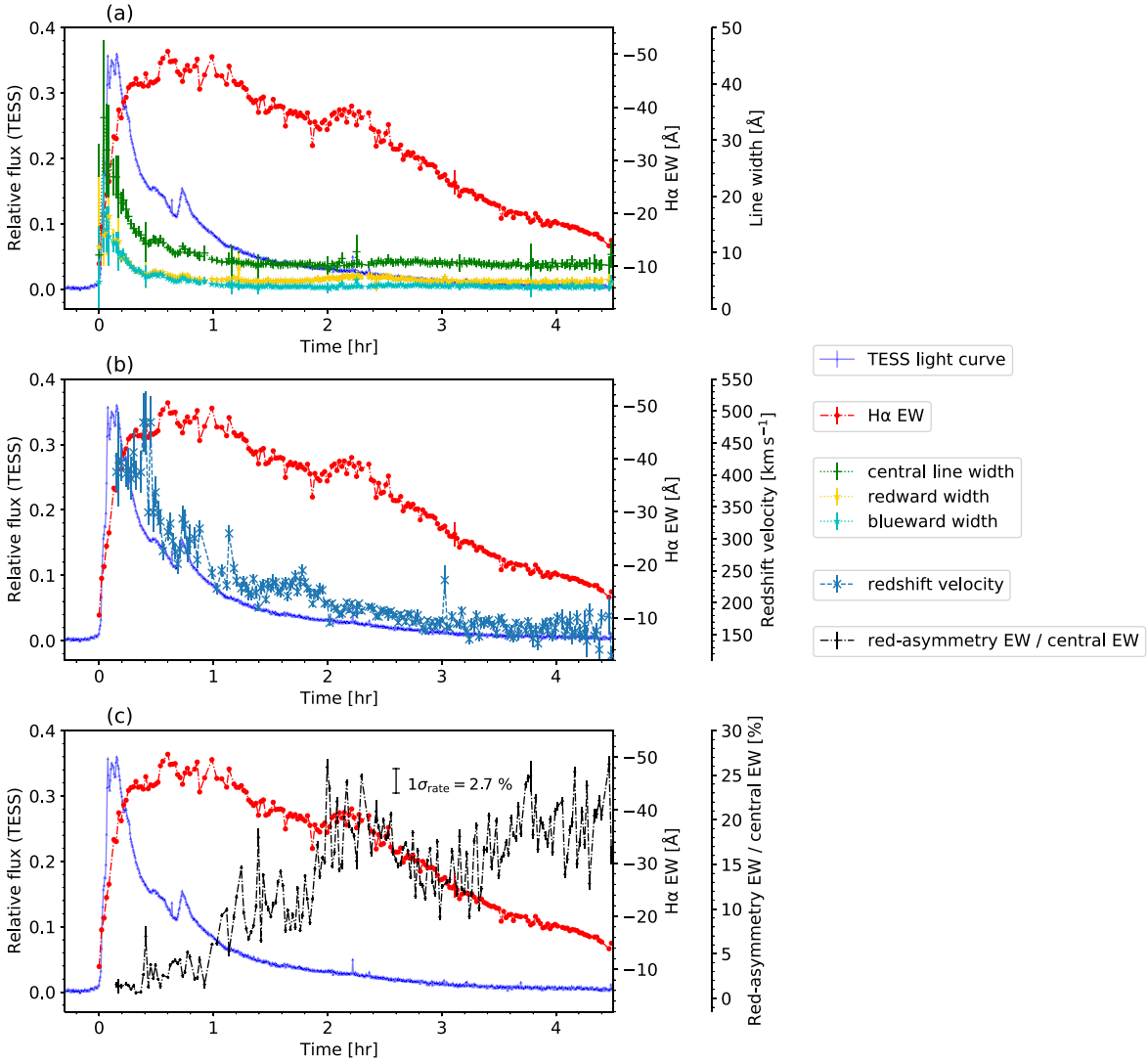


**Figure 5.** Hα line width (a), redshift velocity (b), and the EW ratio of the red asymmetry to the central component (c). The solid blue line represents the light curve in white light (see Figure 1), and the red dashed–dotted line represents the Hα EW. The horizontal axis represents the time in units of hr. The left and middle vertical axes represent the relative flux normalized by the average flux and the EW in units of Å. They are common in the panels (a), (b), and (c). (a) The dotted green line with the cross symbols scaled on the rightmost vertical axis indicates the central line width of Hα in units of Å. The dotted yellow and cyan lines with the star symbols represent the line widths of the red and blue sides, respectively (i.e., 2 × cyan = green). The error bars are calculated using the fitting errors as the uncertainties. (b) The dashed dark cyan line with the cross symbols scaled on the rightmost vertical axis indicates the line-of-sight velocity of the redshifted excess components (derived from the central wavelength of the dashed black line in Figure 4), with the error bars calculated from the fitting errors. (c) The black dashed–dotted line with the diamond symbols scaled on the rightmost vertical axis indicates the ratio of the EW of the redshifted excess components to the Hα EW, with the error bars calculated from the fitting errors. The $1\sigma_{\rm rate}$ error bar is the standard deviation of the residuals, calculated from the moving average. The data after 4.5 hr are not plotted, since the fitting could not be conducted well, because of the weak Hα emission. In addition, the values of the redshift velocity (b) and the ratio of the EW (c) within 9 minutes of the flare's onset are also excluded, because the values obtained from the second fitting to the redshifted components were not reliable, due to the large variances of the residuals.

flares, which lasts for a few tens of seconds to 10 minutes at the most (Xu et al. 2006; Kawate et al. 2016), we do not expect this to represent the decreasing flare heating at a given flare kernel, but rather expect it to represent the decreasing flare heating of the flare ribbons moving outward, as a result of successive reconnection.

### 3.3. Interpretation of Red Asymmetry

In this section, we discuss the origin of the red asymmetry during our superflare. As shown in Section 3.1, red asymmetry with a large velocity of $482 \pm 40$ km s$^{-1}$ was observed during the impulsive phase, and it decayed more rapidly, over 1.6–2.3 hr, than the Hα EW (over 4.0–4.5 hr). The velocity of the redshifted excess components slows down on a timescale similar to those of the white-light emission and line broadening (Figure 5(b)). As discussed in Section 3.2, the evolutions of both the white-light emission and the line broadening could be related to that of the chromospheric condensation region. Hence, this similarity indicates that the chromospheric condensation could be the origin of the red asymmetry, especially in the impulsive phase. In the case of solar flares, it is often observed that the velocities of redshifted components peak out and decay more rapidly than the Hα intensities in the footpoints (i.e., the chromospheric condensation regions; Ichimoto & Kurokawa 1984). This is considered to indicate the properties of the chromospheric condensation process,

where the thickness of the chromospheric condensation increases with the rapid decrease of its velocity (Livshits et al. 1981; Somov et al. 1982; Ichimoto & Kurokawa 1984; Kowalski et al. 2022a). Likewise, in our superflare, the velocity of the redshifted components also decays more promptly than the H$\alpha$ EW, which supports the possibility of the chromospheric condensation being the origin of the red asymmetry.

The initial velocity of the redshifted components, $482 \pm 40$ km s$^{-1}$, is faster than that of the red asymmetry in solar flares ($\leqslant$100 km s$^{-1}$; e.g., Ichimoto & Kurokawa 1984; Asai et al. 2012). In the case of stellar flares, the typical redshift velocity is 100–200 km s$^{-1}$ (e.g., Houdebine et al. 1993; Wu et al. 2022). Koller et al. (2021) have analyzed the asymmetries of H$\alpha$ lines during flares on M-type stars and detected maximum velocities of 358 km s$^{-1}$. Compared to these studies, the observed initial velocity of the redshifted components is relatively fast. In numerical simulations, assuming high–electron beam fluxes that are associated with active M-dwarf flares, most studies show that the downward velocity of the chromospheric condensation is at most $\sim$100 km s$^{-1}$ (Allred et al. 2006; Kowalski et al. 2017a, 2022b). Longcope (2014) has investigated the atmospheric response to extremely high-flux beams in numerical simulations and suggested the possibility of the fast condensation velocity being 100–1000 km s$^{-1}$. Therefore, the observed redshift velocity of 200–500 km s$^{-1}$ in our superflare can be still explained by the chromospheric condensation model, with large energy inputs. However, note that the observed fast velocities could possibly be due to the two-component fitting method that is employed in this study, since it has been pointed out that this method tends to overestimate the velocity (Namekata et al. 2022a). For example, the peak velocity of $\sim$482 km s$^{-1}$ is expected to be roughly overestimated by the redward line width of 6.2 Å (288 km s$^{-1}$). Considering this overestimation, the actual maximum redshift velocity may be $\sim$200 km s$^{-1}$, at most. In any case, the uncertainty does not affect the qualitative discussion, since the trend of the time variation does not change, even if the velocity of the redshifted components has been overestimated.

After the impulsive phase, the red asymmetry in H$\alpha$ still lasts for 4.6–5.1 hr after the flare's onset, with a velocity of $\sim$150–300 km s$^{-1}$ (Figures 3(d) and 5). In addition, Figure 5(c) shows that the EW ratio of the red asymmetry to the central component significantly increases 1–3 hr from the flare's onset, after the EW of the central component has decayed. If the main source of the red asymmetry in the decay phase (>1 hr) is also the additionally heated chromospheric condensation region, we would expect to see an increase of the blueward line broadening and white-light enhancement. However, as shown in Figure 5(a), there are no additional increases in the blueward line broadening and white-light emission during the decay phase, as only the redward line broadening increases. Therefore, it is possible that a physical mechanism other than chromospheric condensation is at work, especially in the decay phase. We suggest that the red asymmetry seen in the late phase of our superflare might be explained by post-flare loops. Harra-Murnion et al. (1998) have reported that some solar flares maintain post-flare loops in H$\alpha$ for more than several hr. Furthermore, recent simulations have suggested that it takes $\sim$30–40 minutes for typical flare loops to cool down to $\sim 10^4$ K (Cargill & Bradshaw 2013; Reep et al. 2020; Ruan et al. 2021). Based on these solar observations, the observed red asymmetry of this superflare—which lasted for several hr and was delayed by $\sim$1 hr compared to the impulsive phase—could be representative of the nature of post-flare loops.

## 4. Summary and Future Works

We performed simultaneous optical spectroscopic and photometric observations of an active M-type flare star, YZ CMi, and successfully detected a superflare with energy of $1.3^{+1.6}_{-0.6} \times 10^{34}$ erg and a duration of 4.6–5.1 hr. Since the number of spectroscopic observations of superflares is still small, our observations, with a high time cadence and high precision, are precious in terms of revealing the superflare mechanism.

During the initial phase, significant line broadenings of the H$\alpha$ line, with widths of up to $34 \pm 14$ Å, are observed, indicating the dense chromospheric region being heated by high-flux nonthermal electron beams. The temporal evolution of the line broadening shows a good correspondence with that of the white-light flare, which means that the white-light emission is also radiated from the nonthermally heated chromosphere in this superflare. In addition, red asymmetry was observed in the H$\alpha$ line, almost throughout the flare. The velocity of the redshifted excess components, with an initial velocity of $482 \pm 40$ km s$^{-1}$, slows down on a timescale similar to those of the white-light emission and line broadening, and decays more rapidly than the H$\alpha$ EW. These indicate the possibility of the chromospheric condensation being the origin of the observed white-light emissions and red asymmetry in the impulsive phase. On the other hand, during the late phase, the post-flare loops could also contribute to the red asymmetry, since the EW ratio of the red asymmetry to the central component increases as the flare decays. Our simultaneous spectroscopic and photometric observations provide further constraints on the mechanism that is responsible for the red asymmetry during (super)flares.

Moreover, the light curves of the white light and H$\alpha$ show several secondary peaks during the flare (e.g., Figure 2(a)). Interestingly, the white-light emission of this superflare showed quasi-periodic pulsations (QPPs; e.g., Kane et al. 1983) in its light curve, although we do not analyze them in this paper. In future work, we will compare the QPPs of white-light flares and the time variations of H$\alpha$ lines. In addition, since most of the previous solar observations referred to in this paper have focused on spatially resolved information for a small portion of the solar disk, we do not know in detail how the H$\alpha$ line profile behaves when solar flares are spatially integrated on the Sun seen as a star (see Namekata et al. 2022a; Otsu et al. 2022). Therefore, in the future, we will conduct Sun-as-a-star analyses not only of flare kernels, but also of post-flare loops, in order to improve the interpretations of the stellar data in this paper.

Finally, we briefly comment on a possible relationship between our superflares and stellar coronal mass ejections (CMEs). CMEs are phenomena that carry plasmas into interplanetary space, by ejecting plasmas upward through the release of magnetic energy, and they are thought to have a significant impact on planetary habitability and stellar evolution (e.g., Aarnio et al. 2011; Drake et al. 2013; Airapetian et al. 2020). Some studies have reported that stellar flares sometimes show blueshifted emission or absorption profiles in the H$\alpha$ line (e.g., Vida et al. 2019; Maehara et al. 2021; Namekata et al. 2021). These are often interpreted as stellar prominence eruptions, which provide indirect evidence of CMEs. In our superflare, only strong redshifted components are observed, and significant blueshifted components were not observed at any

time during the flare. In addition, since a white-light flare was observed, it is speculated that the flare footpoints were on the visible side of the stellar hemisphere. Thus, the possibility of a backward-directed CME relating to a flare occurring close to the limb is unlikely for our superflare. There could be a possibility that the strong overlying magnetic fields of the M dwarf may have suppressed a prominence eruption and CME, resulting in a significant reduction of the velocity (Alvarado-Gomez et al. 2018). Moreover, it is possible that the strong chromospheric condensation during the impulsive phase of this superflare could have masked the faint blueshifted components that are associated with weak CMEs (Koller et al. 2021; Otsu et al. 2022). We expect that a larger sample of time-resolved spectroscopic observations, like those in this study, and simultaneous observations of the X-ray and UV bands will reveal more details about the relationships between redshifts (and blueshifts) and CMEs on stars in the future.

This study makes use of data obtained through the programs 21A-N-CN03 and 21A-K-0009 in open use of the observing time at the 3.8 m Seimei telescope, provided by NAOJ. Funding for the TESS mission is provided by NASA's Science Mission directorate. We acknowledge the International Space Science Institute and the supported International Team 464: The Role of Solar and Stellar Energetic Particles on (Exo) Planetary Habitability (ETER-NAL; http://www.issibern.ch/teams/exoeternal/). Y.N. was supported by the JSPS Overseas Research Fellowship Program. This research is supported by JSPS KAKENHI grant Nos. 18J20048, 21J00316 (K.N.), 21J00106 (Y.N.), and 21H01131 (M.H., D.N., and K.S.). Y.N. was also supported by NASA ADAP award program No. 80NSSC21K0632 (PI: Adam Kowalski).

## ORCID iDs

Kosuke Namekata https://orcid.org/0000-0002-1297-9485
Hiroyuki Maehara https://orcid.org/0000-0003-0332-0811
Yuta Notsu https://orcid.org/0000-0002-0412-0849
Satoshi Honda https://orcid.org/0000-0001-6653-8741
Daisaku Nogami https://orcid.org/0000-0001-9588-1872
Kazunari Shibata https://orcid.org/0000-0003-1206-7889

## References

Aarnio, A. N., Stassun, K. G., Hughes, W. J., & McGregor, S. L. 2011, SoPh, 268, 195
Airapetian, V. S., Barnes, R., Cohen, O., et al. 2020, IJAsB, 19, 136
Airapetian, V. S., Glocer, A., Gronoff, G., Hebrard, E., & Danchi, W. 2016, NatGe, 9, 452
Allred, J. C., Hawley, S. L., Abbett, W. P., & Carlsson, M. 2006, ApJ, 644, 484
Alvarado-Gomez, J. D., Drake, J. J., Cohen, O., Moschou, S. P., & Garraffo, C. 2018, ApJ, 862, 93
Asai, A., Ichimoto, K., Kitai, R., Kurokawa, H., & Shibata, K. 2012, PASJ, 64, 20
Bruzek, A. 1964, ApJ, 140, 746
Candelaresi, S., Hillier, A., Maehara, H., Brandenburg, A., & Shibata, K. 2014, ApJ, 792, 67
Canfield, R. C., Penn, M. J., Wulser, J.-P., & Kiplinger, A. L. 1990, ApJ, 363, 318
Cargill, P. J., & Bradshaw, S. J. 2013, ApJ, 772, 40
Chang, S.-W., Byun, Y.-I., & Hartman, J. D. 2015, ApJ, 814, 35
Claes, N., & Keppens, R. 2019, A&A, 624, A96
Claes, N., Keppens, R., & Xia, C. 2020, A&A, 636, A112
Davenport, J. R. A. 2016, ApJ, 829, 23
Dennis, B. R., & Zarro, D. M. 1993, SoPh, 146, 177
Drake, J. J., Cohen, O., Yashiro, S., & Gopalswamy, N. 2013, ApJ, 764, 170
Emslie, A. G., Dennis, B. R., Shih, A. Y., et al. 2012, ApJ, 759, 71
Fisher, G. H., Canfield, R. C., & McClymont, A. N. 1985, ApJ, 289, 414
Fuhrmeister, B., Czesla, S., Schmitt, J. H. M. M., et al. 2018, A&A, 615, A14
Gaidos, E., & Mann, A. W. 2014, ApJ, 791, 54
Hanaoka, Y. 2003, ApJ, 596, 1347
Harra-Murnion, L. K., Schmieder, B., van Driel-Gesztelyi, L., et al. 1998, A&A, 337, 911
Hawley, S. L., Davenport, J. R. A., Kowalski, A. F., et al. 2014, ApJ, 797, 121
Hawley, S. L., & Fisher, G. H. 1992, ApJS, 78, 565
Houdebine, E. R., Foing, B. H., Doyle, J. G., & Rodono, M. 1993, A&A, 274, 245
Houdebine, E. R., Mullan, D. J., Paletou, F., & Gebran, M. 2016, ApJ, 822, 97
Howard, W. S., Corbett, H., Law, N. M., et al. 2020, ApJ, 902, 115
Hudson, H. S., Wolfson, C. J., & Metcalf, T. R. 2006, SoPh, 234, 79
Ichimoto, K., & Kurokawa, H. 1984, SoPh, 93, 105
Janssens, T. J., & White, K. P. I. 1970, SoPh, 11, 299
Johns-Krull, C. M., Hawley, S. L., Basri, G., & Valenti, J. A. 1997, ApJS, 112, 221
Kane, S. R., Kai, K., Kosugi, T., et al. 1983, ApJ, 271, 376
Kawate, T., Ishii, T. T., Nakatani, Y., et al. 2016, ApJ, 833, 50
Koller, F., Leitzinger, M., Temmer, M., et al. 2021, A&A, 646, A34
Kowalski, A. F., Allred, J. C., Carlsson, M., et al. 2022a, ApJ, 928, 190
Kowalski, A. F., Allred, J. C., Carlsson, M., et al. 2022b, ApJ, 928, 190
Kowalski, A. F., Allred, J. C., Daw, A., Cauzzi, G., & Carlsson, M. 2017a, ApJ, 836, 12
Kowalski, A. F., Allred, J. C., Uitenbroek, H., et al. 2017b, ApJ, 837, 125
Kowalski, A. F., Hawley, S. L., Carlsson, M., et al. 2015, SoPh, 290, 3487
Kowalski, A. F., Hawley, S. L., Hilton, E. J., et al. 2009, AJ, 138, 633
Kowalski, A. F., Hawley, S. L., Holtzman, J. A., Wisniewski, J. P., & Hilton, E. J. 2010, ApJL, 714, L98
Kowalski, A. F., Hawley, S. L., Wisniewski, J. P., et al. 2013, ApJS, 207, 15
Kowalski, A. F., Mathioudakis, M., Hawley, S. L., et al. 2016, ApJ, 820, 95
Kretzschmar, M. 2011, A&A, 530, A84
Krucker, S., Hudson, H. S., Jeffrey, N. L. S., et al. 2011, ApJ, 739, 96
Kurita, M., Kino, M., Iwamuro, F., et al. 2020, PASJ, 72, 48
Lacy, C. H., Moffett, T. J., & Evans, D. S. 1976, ApJS, 30, 85
Livshits, M. A., Badalyan, O. G., Kosovichev, A. G., & Katsova, M. M. 1981, SoPh, 73, 269
Longcope, D. W. 2014, ApJ, 795, 10
Machado, M. E., Emslie, A. G., & Avrett, E. H. 1989, SoPh, 124, 303
Maehara, H., Notsu, Y., Namekata, K., et al. 2021, PASJ, 73, 44
Maehara, H., Shibayama, T., Notsu, S., et al. 2012, Natur, 485, 478
Matsubayashi, K., Ohta, K., Iwamuro, F., et al. 2019, PASJ, 71, 102
Morin, J., Donati, J.-F., Petit, P., et al. 2008, MNRAS, 390, 567
Najita, K., & Orrall, F. Q. 1970, SoPh, 15, 176
Namekata, K., Ichimoto, K., Ishii, T. T., & Shibata, K. 2022a, ApJ, 933, 209
Namekata, K., Maehara, H., Honda, S., et al. 2022b, ApJL, 926, L5
Namekata, K., Maehara, H., Honda, S., et al. 2021, NatAs, 6, 241
Namekata, K., Maehara, H., Sasaki, R., et al. 2020, PASJ, 72, 68
Namekata, K., Sakaue, T., Watanabe, K., et al. 2017, ApJ, 851, 91
Neupert, W. M. 1968, ApJL, 153, L59
Newton, E. R., Charbonneau, D., Irwin, J., & Mann, A. W. 2015, ApJ, 800, 85
Nizamov, B. A. 2019, MNRAS, 489, 4338
Notsu, Y., Maehara, H., Honda, S., et al. 2019, ApJ, 876, 58
Notsu, Y., Shibayama, T., Maehara, H., et al. 2013, ApJ, 771, 127
Okamoto, S., Notsu, Y., Maehara, H., et al. 2021, ApJ, 906, 72
Otsu, T., Asai, A., Ichimoto, K., Ishii, T. T., & Namekata, K. 2022, ApJ, 939, 98
Priest, E. R., & Forbes, T. G. 2002, A&ARv, 10, 313
Reep, J. W., Antolin, P., & Bradshaw, S. J. 2020, ApJ, 890, 100
Ricker, G. R., Winn, J. N., Vanderspek, R., et al. 2015, JATIS, 1, 014003
Ruan, W., Zhou, Y., & Keppens, R. 2021, ApJL, 920, L15
Shibata, K., Isobe, H., Hillier, A., et al. 2013, PASJ, 65, 49
Shibata, K., & Magara, T. 2011, LRSP, 8, 6
Shibata, K., & Yokoyama, T. 2002, ApJ, 577, 422
Shibayama, T., Maehara, H., Notsu, S., et al. 2013, ApJS, 209, 5
Somov, B. V., Sermulina, B. J., & Spektor, A. R. 1982, SoPh, 81, 281
Soubiran, C., Jasniewicz, G., Chemin, L., et al. 2018, A&A, 616, A7
Svestka, Z. 1962, BAICz, 13, 236
Svestka, Z. 1963, BAICz, 14, 234
Švestka, Z., Kopecký, M., & Blaha, M. 1962, BAICz, 13, 37
van Maanen, A. 1945, PASP, 57, 216
Vida, K., Leitzinger, M., Kriskovics, L., et al. 2019, A&A, 623, A49
Wu, Y., Chen, H., Tian, H., et al. 2022, arXiv:2203.02292
Xu, Y., Cao, W., Liu, C., et al. 2006, ApJ, 641, 1210
Yamashiki, Y. A., Maehara, H., Airapetian, V., et al. 2019, ApJ, 881, 114